Absolute effective areas of the HETGS

N.S. Schulz, D. Dewey, H.L. Marshall

Center for Space Research, M.I.T., Cambridge, MA 02139

ABSTRACT

XRCF measurements of the flight AXAF High Energy Transmission Grating Spectrometer throughput were used to determine absolute effective areas. The results are compared with component models of the HRMA, HETG, and the ACIS-S. The comparison provides an independent view on HETG efficiencies as well as the detector efficiencies along the dispersion direction. Using the XRCF double crystal monochromator measurements in the range from 0.9 to 8.7 keV, the effective areas in the 1st order MEG were determined with an accuracy of better than 10%, in the 1st order HEG better than 15% throughout most of the energy range. This is within the goal set for the XRCF measurements to refine state of the art composite component model predictions, which in future will allow us to draw conclusions on the in-flight HETGS absolute effective area.

Keywords: X-ray, diffraction, grating, calibration, CCD, monochromator, spectroscopy

1. INTRODUCTION

The High-Energy Transmission Grating Spectrometer (HETGS) onboard NASA's Advanced X-ray Astrophysics Facility (AXAF) is designed to perform high resolution X-ray spectroscopy with spectral resolving power of up to $E/dE \sim 1000$ in the 0.5 to 10 keV energy band. The HETGS results from the combined operation of the High Resolution Mirror Assembly (HRMA), the High-Energy Transmission Grating (HETG), which can be inserted into the optical path just behind the mirror assembly, and the AXAF CCD Imaging Spectrometer array (ACIS-S) located in the AXAF focal plane. As a backup configuration the spectrometer could also operate with the High Resolution Camera (HRC-I) in the focal plane. Detailed descriptions of the HETGS have been given previously in these conferences,[10,6,11] but we also want to encourage the interested reader to consult the AXAF Observatory Guide[13] for a general overview of AXAF and the HETGS WWW site (see note below) for up-to-date information about the HETGS. The latter site also features all the relevant input calibration products used for this analysis with the relevant references.

The central parts of the spectrometer are the two sets of high-energy transmission gratings, Medium Energy Grating (MEG) facets of 4000 Åperiod and High Energy Grating (HEG, 2000 Åperiod) facets, which together form the High-Energy Transmission Grating (HETG). Figure 1 shows a photo of the HETG flight instrument. It consists of four concentric rings tiled with grating facets, each ring intercepts the optical path of the corresponding type-I Wolter mirror pair of the HRMA in order to diffract the X-rays before they hit the focal plane. X-rays feeding the MEG come from the two outer HRMA shells 1 and 3, which by design are optimized for effective area in the lower part of the AXAF energy band. The HEG intercepts X-rays from the two inner shells, which are optimized towards the higher energies. The orientation of the dispersion axis of MEG and HEG are offset by approximately 10 degrees, in order to fit the dispersed spectra from both grating types onto one detector array, minimizing any spatial interference between the two.

The HETG has been designed to place each facet at its prescribed location and orientation on a Rowland torus[14,11,10] with a diameter of 8635 mm. Therefore the 'focal plane' of the spectrometer is actually not a plane but an approximation to a portion of the Rowland torus at 8635 mm distance. In order of match that Rowland torus in the focal plane, the detector consists of 6 imaging CCDs in a 1x6 array, which are tilted along the torus. An illustration of the focal plane view is shown in figure 2 using a continuum measurement with the HETGS. For a detailed description of ACIS we refer to reports in this volume[3] and ACIS Team Calibration Report.[2] The CCD array consists of two different types of CCDs, 4 front illuminated devices (FI) and 2 back illuminated devices (BI),

Other author information: Send correspondence to N.S. Schulz.: Email: nss@space.mit.edu; Telephone: 617-258-5767; Fax: 617-253-8084
Up-to-date information available at: **http://space.mit.edu/HETG/xrcf.html**

which are arranged in an array denominated from S0 to S5 (going from -Y to +Y in AXAF coordinates), in the illustration from left to right. S1 and S3 are the two BI devices. The position of the 0th order image, which for HEG and MEG coincides where the two dispersed continua cross each other and marked by the small black box, is on the back-illuminated device S3. This will also be the a launch locked focal position for AXAF.

2. DEFINITIONS AND INPUT CALIBRATION PRODUCTS

The HETGS effective area in general consists of 3 contributing elements, the HRMA single shell effective areas (A_s), the effective HETG grating efficiencies (G_s) for the mirror shells, and the ACIS-S photon detection efficiencies (QE_{acis}),

$$A_{hetgs}(E, m, \text{mode}) = \sum_{s=1,3,4,6} A_s(E)\ G_s(E,m)\ QE_{acis}(E, \vec{X}, \text{mode}). \tag{1}$$

Here E denotes the dependence on energy, m the diffraction order, *mode* the event identification in the CCD (here, for example, we will consistently use the sum of ASCA grades 0,2,3,4,6 and TE-mode), and the $\vec{X}$ dependences from spatial dependencies in the detector array, i.e FI/BI efficiencies and gap locations between the devices.

Figure 3 shows the total AXAF HRMA on-axis effective area at XRCF and its contributing single shell areas. Mirror shells 1 and 3 cut off at energies around 5 and 6.5 keV, while shells 4 and 6 extend up to 7 and 9 keV. The decrease near 2 keV is due to the iridium M-edge in the reflective mirror coating. The effective area sum, equation 1 above, then adds s = 1 and 3 for the MEG area and 4 and 6 for the HEG area.

In general each CCD device has its own characteristics. However, since not all quantum efficiency functions are yet avalable, we have to use templates for each CCD type. Figure 4 shows the quantum efficiencies for the FI device in I3 of the imaging array versus the BI device in S3 of the spectroscopy array. The functions already include the transmission characteristics of the flight filters. The use of these templates is reasonable since FI devices are quite similar and we only expect systematic deviations of the order of 5%. The difference between the two BI devices (S1, S3) should not be significantly larger. However, as we will show during the analysis, the differences are visible in the data.

The grating efficiencies have been determined at the X-Ray Grating Evaluation Facility (X-GEF) at MIT.[5,7] The diffraction efficiency of each flight grating was measured at several energies and orders and positions within each facet. Figure 5 show the efficiencies for MEG and HEG. Displayed are the zeroth order (solid line) and the 1st and 3rd positive order in MEG, and the 1st and 2nd order in HEG, which are the dominant orders for each grating.

3. MEASUREMENTS AT XRCF

In April 1997 the HETGS underwent extensive testing at the X-Ray Calibration Facility (XRCF) at the Marshall Space Flight Center (MSFC).[16,17] The measurements designed for HETGS effective area calibration were performed using a variety of X-ray sources and detectors in order to cover the whole effective energy range with high resolution lines of sufficient power.[6] In this article we focus on measurements performed with the Double Crystal Monochromator (DCM), in which an energy range of 0.9 to 8.7 keV was covered. During this phase "H" of XRCF testing the ACIS-S array was the only flight detector in the focal plane for these set of measurements. The setup also included several Beam Normalization Detectors (BNDs), here we make use of the four BNDs positioned at the HRMA entrance plane.

3.1. DCM characteristics

The DCM is part of the X-ray Source System (XSS) used at XRCF.[15,9] It offered three 3 different crystals for these tests, of which we only used the Thallium Acis Phthlate (TAP) between 0.9 and 2.5 keV and the germanium (Ge111) between 2.5 and 8.7 keV. The source is a rotating-anode tungsten source, which operates at a high voltage to generate a strong continuum, however it also produces several bright W lines at 1.38, 1.78, and 1.84 keV. Those line actually proved quite useful for test of HETG scattering.[4] The DCM has an energy gradient in dispersion direction, which results in a non-negligible beam non-uniformity when tuned near the the W lines. Another source of non-uniformity is introduced while using the TAP crystal due to some waviness on the crystals surface.

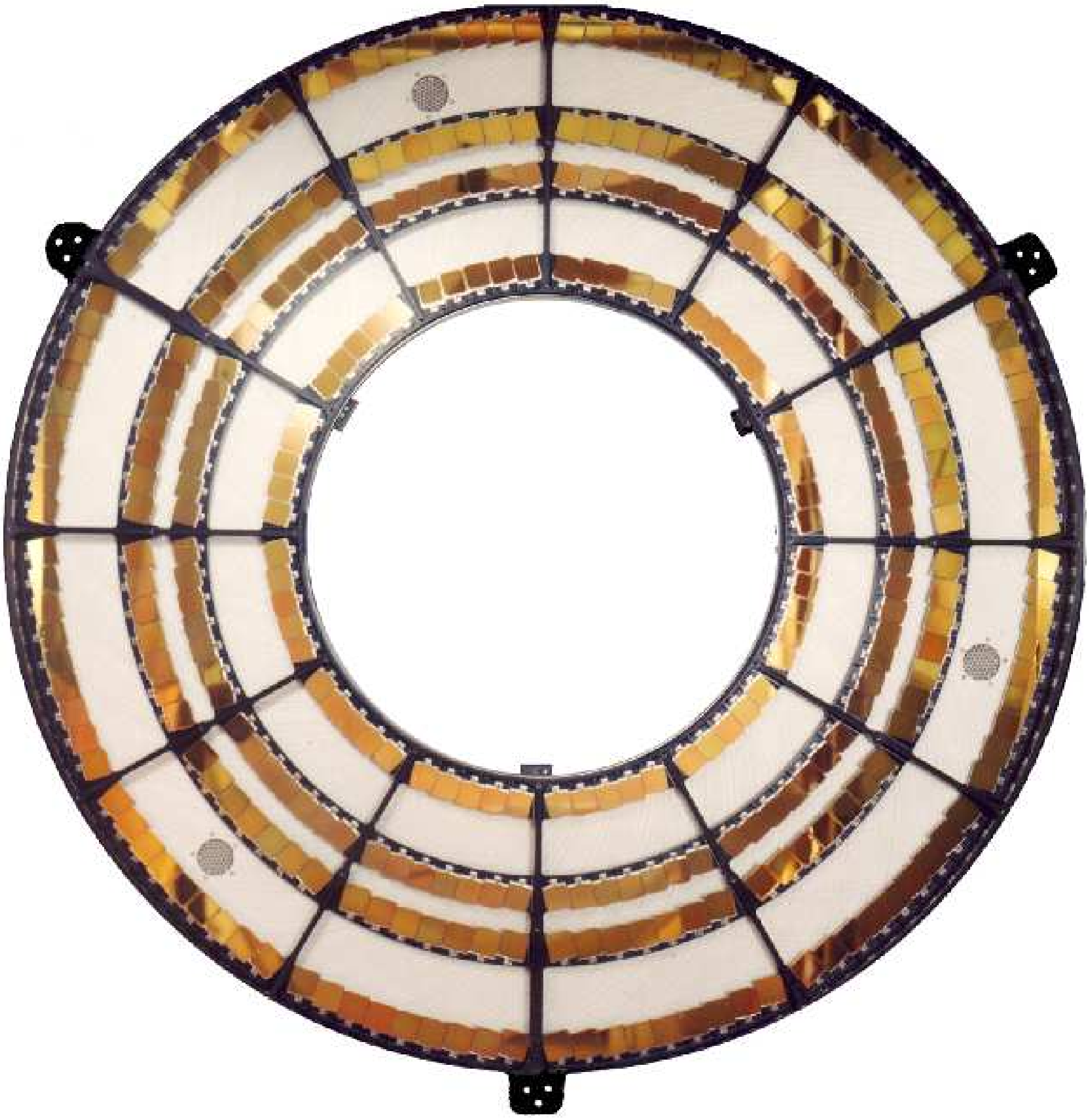

Figure 1. A photograph of the HETG assembly. It is made of 336 grating facets attached to a light-weight aluminum structure. The two outer rings are tiled with MEG facets, the two inner rings have HEG facets.

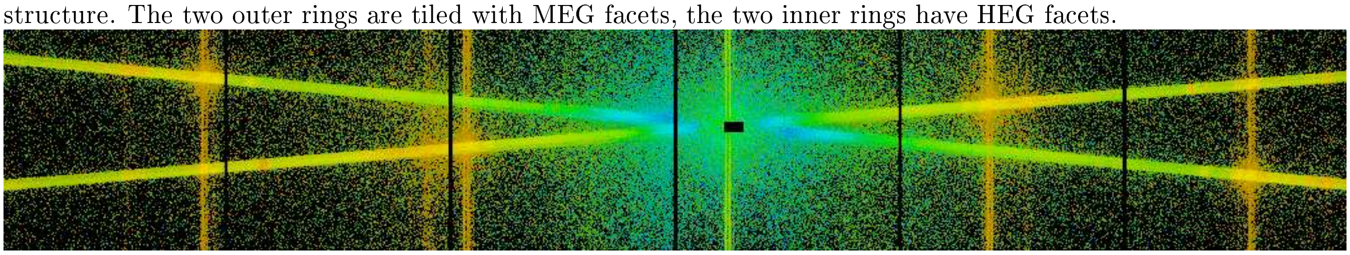

Figure 2. Continuum measurement using the HETGS at XRCF. A unfiltered Cu-anode source produces a broadband X-ray continuum that is spread out along the HEG and MEG dispersion axes. The illustration shows the set-up of the six CCD devices (S0 to S5 from left to right, with the gaps between the devices. The MEG disperses into the upper right (and lower left corner), the HEG into the lower right (upper left corner). The vertical traces that appear at the 0th order image as well as at Cu-L (0.93 keV) are CCD-frame transfer read-out effects.

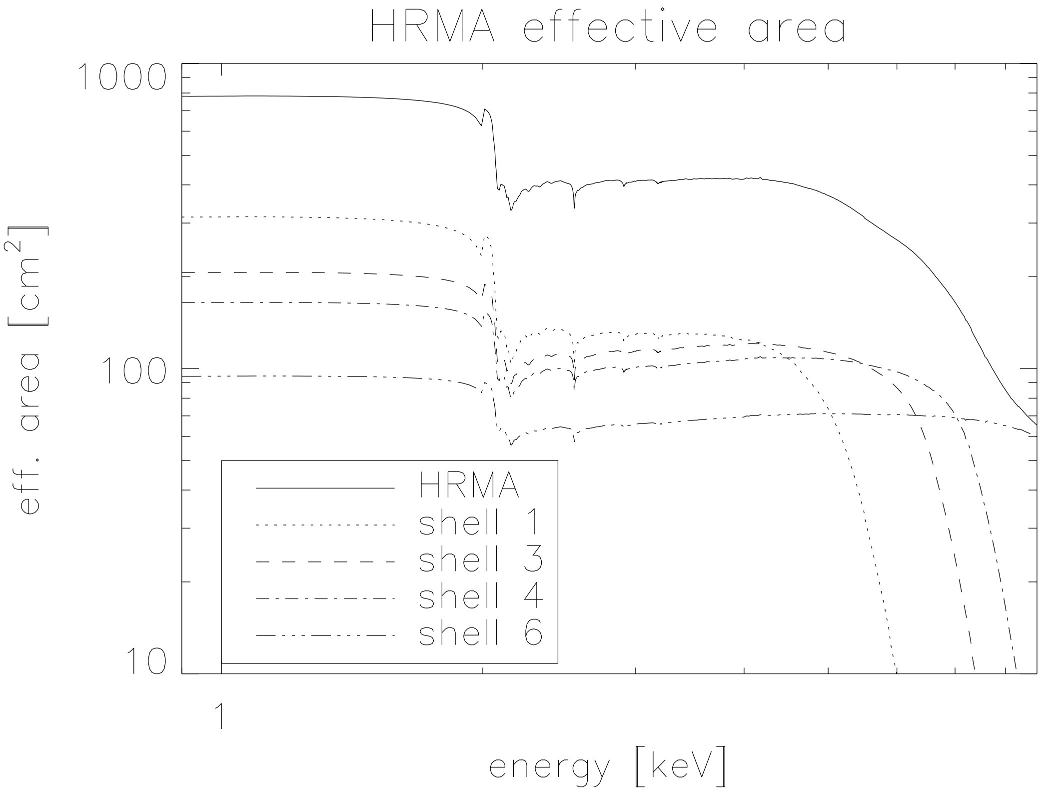

Figure 3. HRMA effective areas, the straight line shows the total area, followed by the ones for each shell (courtesy of the AXAF MST).

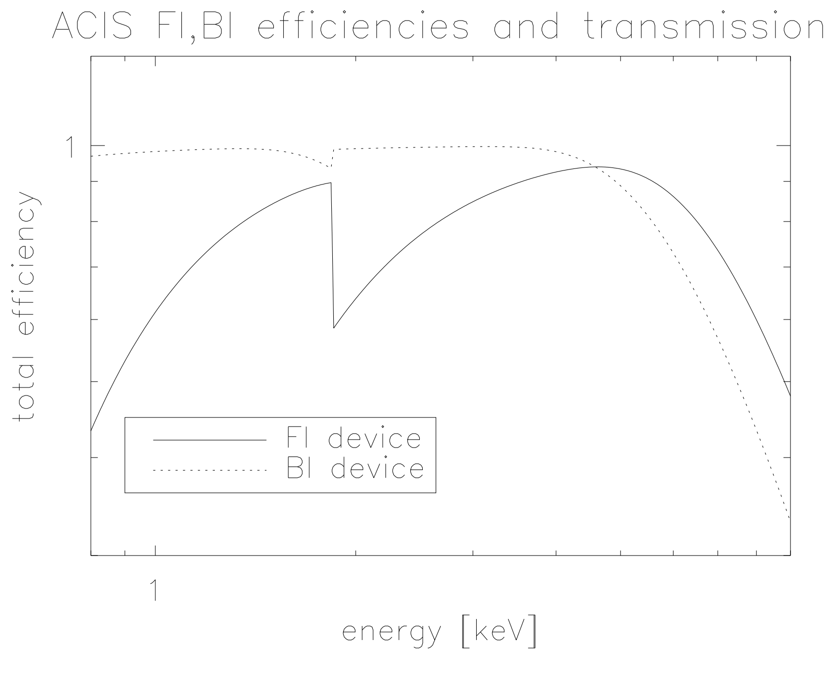

Figure 4. Effective efficiencies (quantum efficiency $\times$ filter transmission) as a function of energy for the FI device I3 in ACIS-I and for the BI device S3 in ACIS-S (courtesy of the MIT ACIS team).

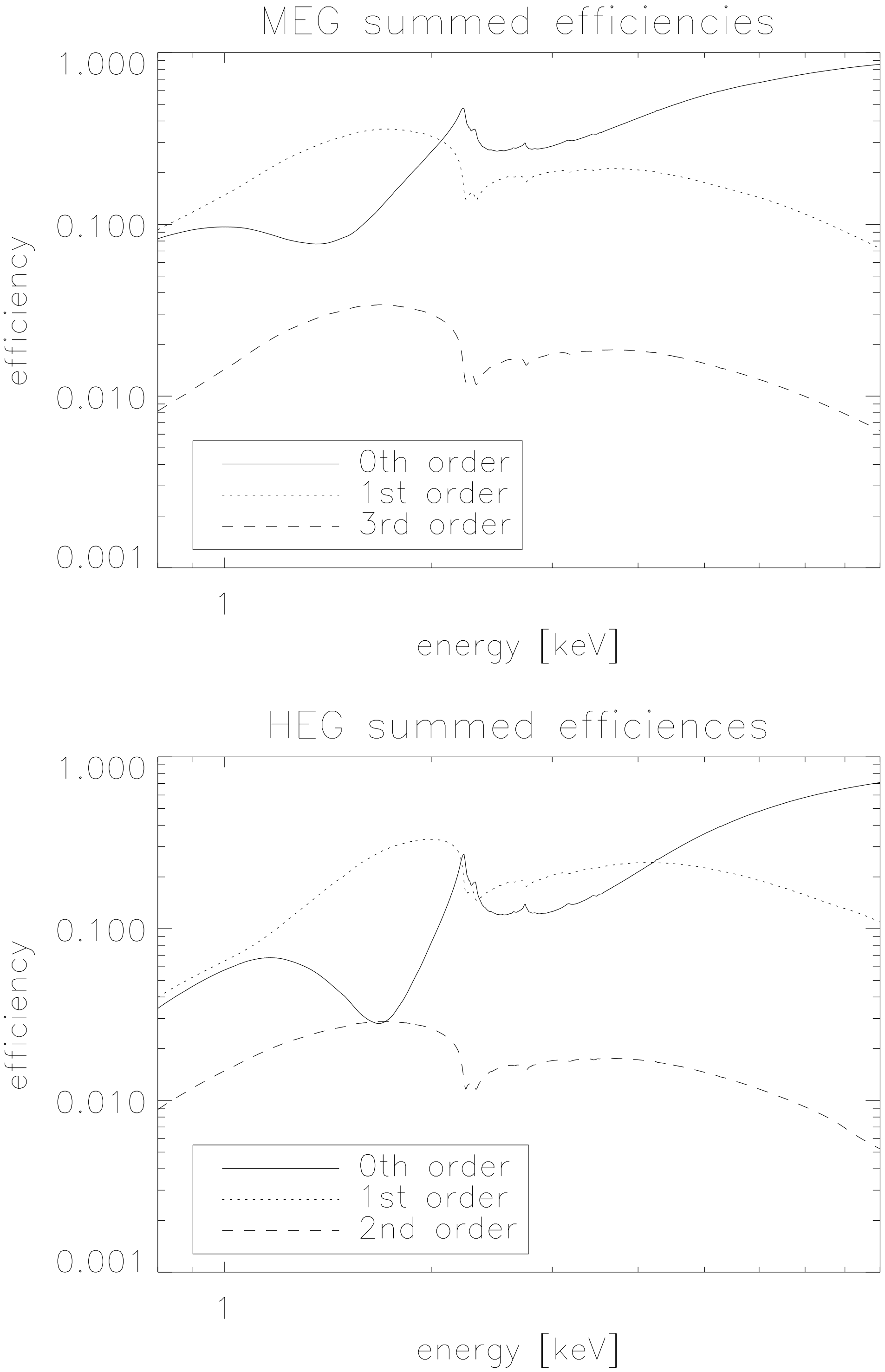

Figure 5. MEG (top) and HEG (bottom) efficiencies as a function of energy, from subassembly data analysis.

TRW-ID H-HAS-EA-	DCM crystal	Energy eV	Increment eV	steps	~cts/step
8.001	TAP	950	50	5	41000
8.002		1200	50	5	45000
8.003		1400	30	11	28000
8.004		1860	20	8	35000
8.005		2050	30	11	12000
8.006	Ge1	2500	150	11	18000
8.007		4000	200	6	18000
8.008		5000	250	9	28000
8.009		7200	500	4	23000

Table 1. List of HETG effective area measurements with the DCM at XRCF. The energies listed are the start energies of each set. Exposure times varied between ~1000 and 2000 s for each energy.

3.2. Energy scans

The energy scans taken with the DCM include a total of 70 steps; Table 1 summarizes these measurements. The measurements were divided into 9 blocks with different increments. The first 2 blocks consisted of 8 steps of 50 eV starting from 950 eV, the next 3 blocks covered an energy range between 1.4 and and 2.4 keV in 30 eV steps, followed by 150 eV steps until 4 keV. The increments were then increased up to 500 eV until 8.7 keV.

In order to get sufficient photon counting statistics in the diffracted orders, the high voltage of the tungsten source was steadily increased above 2.5 keV. The total number of counts for each energy step then varied between 1.1×10^4 to 4.5×10^4 counts. Figure 6 shows a typical measurement, which included 11 steps between 2.5 and 4.0 keV. The detector was moved 40 mm out of focus along the optical axis towards the HRMA in order to spread the focal image over as many detector pixels as possible. The dispersed images appear as rings reflecting the two outer mirror shells in the MEG, the two inner shells (and therefore smaller rings) for the HEG. Each order appears as a sequence of rings separated by the dispersed increment of 150 eV.

The analysis uses DCM measurements only, that is energies above 950 eV. This has one particular shortcoming for the calibration of the HETGS, which is that except for some data from the S0 device in the HEG +1st order, the two outer CCDs S0 and S5 are not in the dispersion range of the bright 1st orders.

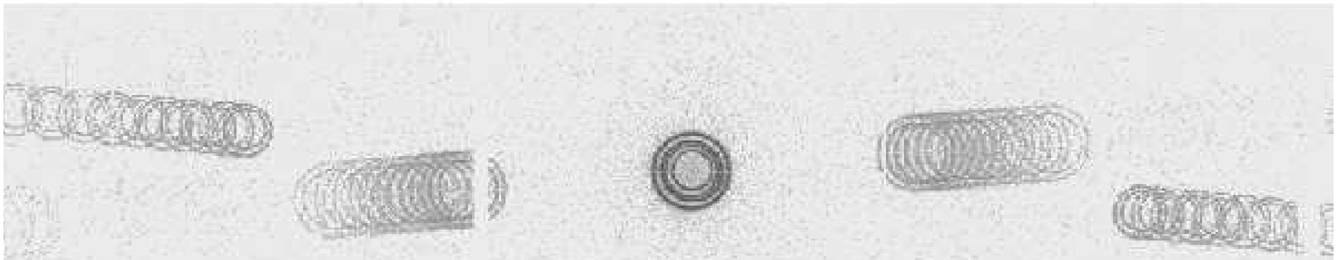

Figure 6. HETGS image of measurement H-HAS-EA-8.006. The image includes MEG and HEG 1st order. Each order consists of 11 steps 150 eV apart

4. DATA REDUCTION

The event lists used for this analysis were provided by the ACIS team at Penn State University, who separated the telemetry data stream into the proper test segments and performed the basic processing of CCD data in terms of bias subtraction and ACIS flight event grading. Starting from the resulting event lists, the further reduction of the data involves several more steps. First of all, the test segments (first column in table 1) still contain a number of energies depending on the the number of DCM steps performed. The single energy events were extracted and written into separate energy lists with a well defined exposure time. Since in this analysis we restrict the event selection to one single grade set, we have to re-grade the data into the sum of ASCA grades 0,2,3,4,6, which are basically a subset of the 255 ACIS flight grades. One then spatially extracts each order by using the grating dispersion relation

$$sin(\theta) = \frac{m\lambda}{p} \tag{2}$$

where m is the order of diffraction (an integer 0, $\pm1, \pm2$, ...), p is the grating period and θ is the dispersion angle. Knowledge of the dispersion axis and the grating-to-detector distance, the Rowland distance, allows a conversion of the angle θ to a physical location on the detector.

Each extracted order has a pulse height spectrum from its location on a particlar CCD. After applying the specific gain correction for each device, ideally we then should see one single peak with a FWHM of the spectral resolution of the device at that particular energy. In reality this is not the case for many reasons and it is crucial to select a proper region of interest to select all the counts that are from the line source only. Generally the flux in the dispersed order is low enough not to cause significant pile-up. Piled-up photons are identified by peaks in the pulse height spectrum at twice the energy for 2 incident photon, three times the energy for 3 incident photons and so on. One major obstacle in this filtering process is, for example, that at energies below 2 keV the first orders in HEG and MEG spatially mix with higher orders of the W lines generated by the DCM. For energies around 1 keV this emission interferes with the first pile-up peak in the pulse height spectra. This especially poses a problem in zeroth order, where pile-up is more significant.

4.1. Beam Normalization

In order to monitor the source flux illuminating the telescope a system of beam nomalization detectors were positioned in the facility.[16] One set was positioned close to the X-ray source, and one set at the entrance plane of the HRMA. For our analysis we are primarily interested n the flux at the HRMA entrance plane; the beam is quite large at that stage, therefore we need to determine the source flux at various position within the beam in order to compensate for non-uniformities in the beam. Four gas flow proportional counters (FPCs) were placed at +Z (FPC-T, top), -Z (FPC-B, bottom), -Y (FPC-N, north), and at +Y (FPC-S, south) od the HRMA aperture at a radial distance of slightly larger than the outer shell radius. The denominations 'top', 'bottom', 'north', and 'south' reflect the actual orientation within the test chamber at XRCF. The analysis of the FPC data for the DCM scans has been performed by the AXAF project scientist team at MSFC. For details of this analysis we refer to the AXAF Project Science Calibration Report and references therein ([12,15]).

Figure 7 shows the flux at the four BNDs during each of the 70 energy steps of the DCM separated into a diagram for lower and for higher energies. The behaviour of the beam flux in the two energy domains is quite different. The reason for this lies in the DCM and its X-ray source. As described above, between 1.3-2.0 keV three prominent lines appear in the spectrum. The intrinsic optical properties of the DCM crucially imprint onto the uniformity of the beam: the lines will appear at only certain angles, which translate to different locations at the HRMA entrance plane. Hence the lines result in strong non-uniformities. The DCM then was tuned in a way that the major gradient in line flux appeared between FPC-S and FPC-N, while the other two remained in reasonable aggreement, i.e only one gradient appeared across the beam. At higher energies the four monitors are well in aggreement, major discontinuities in the flux versus energy flunction appeared only when the crystal type in the DCM was changed.

4.2. Corrections

Two additional corrections have to be applied to the data once each order has been separated and the appropriate pulse height have been selected. One is a pile up correction in the high flux domain. Here it turned out that this was only a severe problem in the 0th order image and details of that analysis will be discussed in the next section below.

The other correction comes from flux losses when a single order hits a gap between CCD devices. The effect is quite prominent when it occurs and the probability that it effects an order near gaps is high since the diameter of an order image is more then 5 mm in the MEG and about half that size in the HEG at 40 mm intrafocal position. Flux losses sometimes amounted up to 45% in the case of the HEG. Therefore every time an image partially hit a gap (the

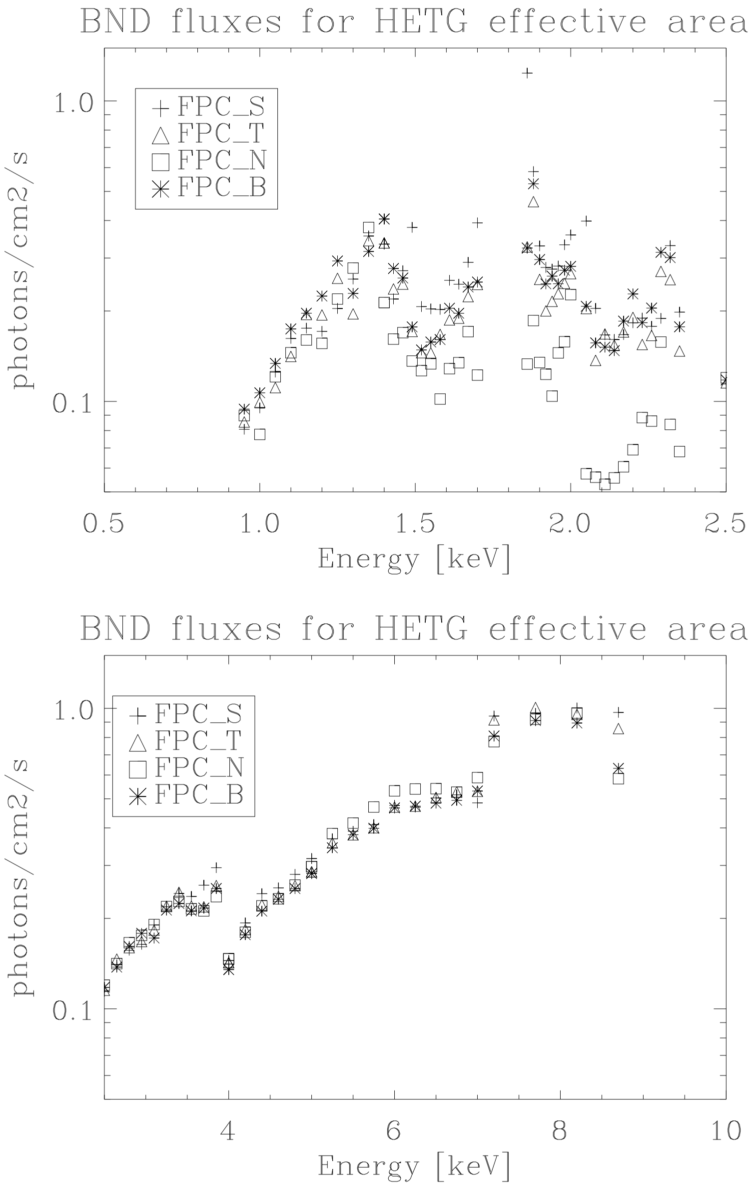

Figure 7. BND flux around the HRMA aperture as a function of energy below and above 2.5 keV .

gap is about 0.43 mm wide) we calculated the portion of the rings (note that at lower energies the image always had 2 rings from 2 contributing shells) and applied this portion as a correction factor to the flux. The method, however, has its flaws, *e.g.* when the gap was between a FI and BI device, which in the low and in the high energy domain have significantly different quantum efficiencies. However, the systematic errors introduced in these domains were less than 1% and thus disregarded.

5. EFFECTIVE AREA ANALYSIS

The measured effective area of an HETG order is the ratio of the count rate of that particular order received by the CCD array to the incident source flux at the HRMA entrance plane:

$$A_{meas}(E_{DCM}, m, \text{mode}) = \frac{\text{focal plane counts/s in order}}{\text{source flux atHRMA}} \quad [\frac{\text{counts/s}}{\text{photons/cm}^2\text{s}} = \text{cm}^2 \frac{\text{counts}}{\text{photon}}] \tag{3}$$

This measured quantity thus depends on the specific analysis methods, such as event identification in the detector array as well as the flux determination method in the BNDs. The uncertainty of the result involves the statistical error of the determined count rates and any statistical and systematic errors from each of the four the BND fits. Another systematic uncertainty is present in the determination of the subassembly grating efficiency measurements shown in figure 5. Those are not included in the uncertainty of the XRCF data. In the higher orders the uncertainty in the measured effective area is dominated by counting statistics.

5.1. Effective area in 0th order

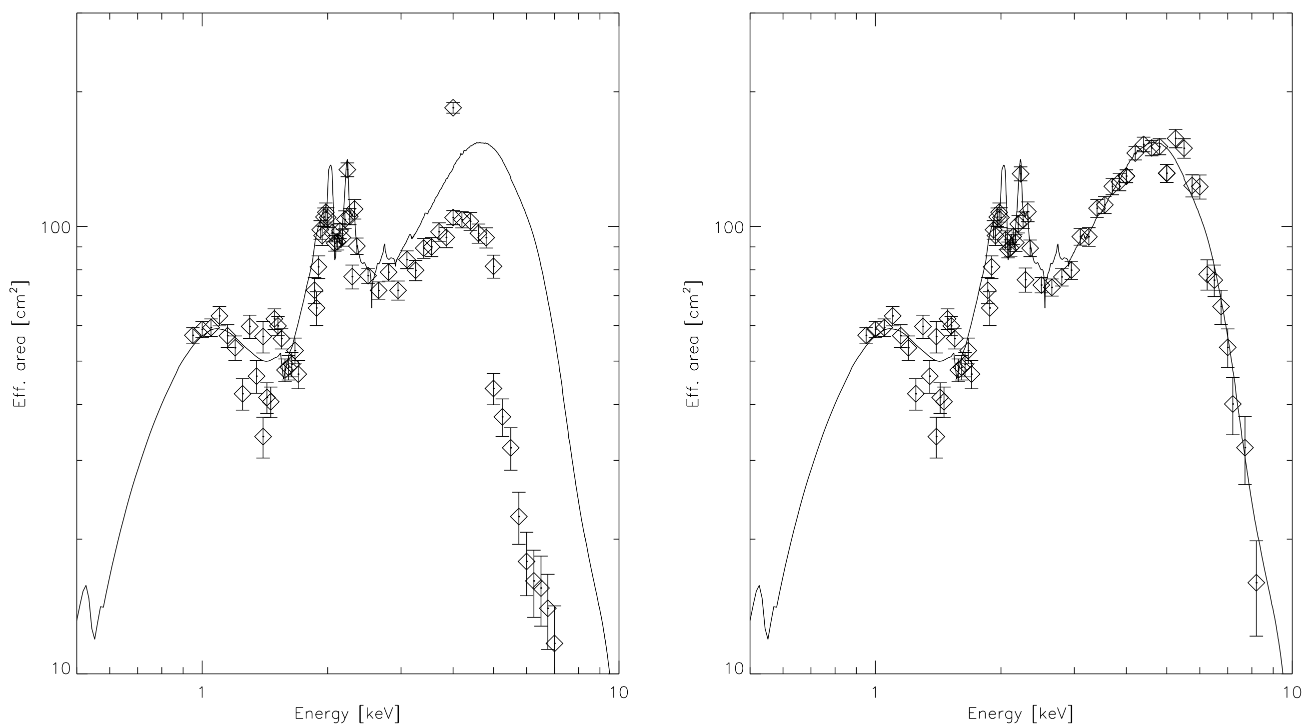

Figure 8. Comparison of the measured and expected effective area for the combined 0th order of MEG and HEG as a function of energy. The left hand diagram shows the result without, the right hand diagram with pile up correction as described in the text.

The treatment of the effective area measurements for the zero order is in many respects different from the ones for 1st and higher orders. First of all, these data sets were not designed for this kind of analysis because in order to get sufficient statistics in the higher orders, the source flux had to be high, especially at high energies. Therefore the zero order data will be entirely dominated by pileup effects in the CCD. Second, we are not able to separate the MEG and HEG incident flux throughout the entire energy band. This is because in order to avoid any confusion of the higher order image rings with each other, the detector array was gradually moved back into the focal plane above 2.5 keV. Figure 6 shows the zero order image as it appeared beween 2.5 and 4.0 keV. The detector here was already moved back from 40 mm out of focus to 20 mm. It is clear that a separation of the inner two rings from the outer ones, in perticluar separating the images of mirror shells 3 and 4, would already introduce a significant systematic uncertainty. Above 4.0 keV, where the out-of-focus position was 10 mm and less, the separation of the inner rings would have become impossible. Therefore we will analyze the zero order data for two reasons: first, we use the low energy domain in order to fine tune the beam normalization in the range between 1.3 and 2.5 keV; second to attempt a pileup treatment using results from the ACIS affective area analysis performed by ASC ACIS team[1] (in this volume).

The top diagram in figure 7 shows quite a strong gradient between FPC-S and FPC-N flux, indicating strong beam non-uniformities. In the range 2.0 - 2.5 keV the FPC-N, however, shows an unsually large drop in flux. In order to minimize these effect on the analysis of the higher orders, we attached constant weights to each of the normalization fluxes in the range between 1.3 and 2.5 keV. Then we simply tuned those weights for each detector until the data in this range matched the values just below 1.3 and just above 2.5 keV. The result is shown in the left diagram of fig 8. For the other portions of the energy band, the normalization flux was simply the average over all four BNDs. Below 1.3 keV we observed an agreement with the expectation of better than 5%, between 1.3 and 2.0 keV the uncertainty is determined by the scatter induced by the BND uncertainties and thus can reach 30%; between 2.0 and 3.0 keV it is again near 5%.

The simplest way to identify pileup is to determine higher order pileup peaks in the pulse height spectrum. For energies below 3 keV it is possible to detect higher order pulse heights corresponding to up to 4 photons hitting the same event detection cell. The corresponding number of counts was summed up and added back to the single photon count rate. The left diagram of figure 8 already includes that summation. Clearly above about 3 keV this procedure starts to fail because higher order pulse heights fall beyond the maximum pulse height channels. Therefore we observe a large drop in the measured effective area. In a first attempt to estimate the amount of piled-up photons we fit the ratio of the non-piled-up fraction to the measured piled-up fraction in the range 0.9 to 2.5 keV. In this range we were able to recover piled-up photons for up to 4 photons hitting an single detection cell. This could be done by a power law of index 0.27. We extrapolated this function into the high energy range and added that flux to the count rate above 2.5 keV. We also had to take in account that the source flux above 2.5 keV increased by a factor of 8 and scaled that function simply by that increase. Since pile-up is actually a stochastic process we could have also estimated the missing higher order counts out of a poissonian distribution. In any case the resulting area was still short of the expectation by up to 45%. Allen et al. 1998 found that some of the piled-up photons migrate into ASCA grade 7, i.e. outside the chosen standard grade set. This results in another energy dependent correction factor. We thus calculated the grade migration correction factor for our data sets follwing the recipe given in[1] and applied it to the data. Again the result above 6 keV was still short by about 20%. Allen et al. 1998 also apply a correction for lost charge and indetected events. Above 6 keV simply applied those correction factors from table 1 in[1] for the case of S3. The result can be seen in the right handed diagram of figure 8. The area now seem to fit the expectation, although a clear overcorrection is visible. However, we have to emphasize, since we did not in particular detemine the lost charge correction for our own data sets, the result is merely an estimation. It however demonstrates that those corrections applied by[1] are indeed necessary and in a reasonable order of magnitude. The applied corrections induce additional systematic errors to the data, which are *not* reflected in the error bars in the right handed diagram of figure 8.

5.2. 1st and 3rd order effective areas for the MEG

The MEG is optimized to supress efficiency in even orders. In the following we do not present results for any even MEG order. The top diagram of figure 5 shows the the subassembly expectation for the sum of the positive and negative 1st and 3rd MEG orders, i.e. in order to apply to single orders one has do divide these values in half. Considering the fact that efficiencies for single 3rd orders are a factor 10 to 20 lower than 0 order efficiencies we should not expect a significant contribution from pile up effects. In the 1st order single side efficiencies, however, we do have to expect a similar amount of piled-up photons at energies below 2.2 keV as we observed in 0th order, since the efficiencies are of comparable magnitude. At higher energies the efficiencies are between a factor 5 and 15 lower, which reduces the probability of pile-up accordingly. In the following we therefore will not apply any other correction than to add all the counts found in detected higher pile up orders in the pulse height spectra.

Figure 9 shows the effective areas determined for the -1st (top, m1) and +1st (bottom, p1) order of the MEG. All data points are confined within 3 CCDs, S2-4. The -1st order covers S2 for all energies below 4.2 keV, and S3 for all higher energies, the 1st order covers S4 for energies below 1.5 keV, and again S3 for all the higher energies. In both orders it is clear that measurements around the tungsten Mα line at 1.75 keV (width $\sim$ 150 eV) have to be disregarded; although we are able to clean the focal plane data from that emission, we cannot entirely do so in the BNDs. Around 1.3 keV we see some scatter in the data, which is also induced by the uncertainty of the BNDs of the order of 10 to 20%. At all other energies, with a few exceptions, we measured the effective area to an accuracy of 5 to 10%. At high energies above 6 keV counting statistics do not allow a determination better than 10%.

We compare these measured effective areas to the expected area distribution from equation 1. To first order we find a remarkable match of the data to the expected distribution. However, there are notable deviations, which are at the limit or exceed the 5% uncertainties of the data points. At +1st order, the very low energy data points stay below the expectation by an amount of somewhat less than 5%. There may be a similar trend in the -1st order, however

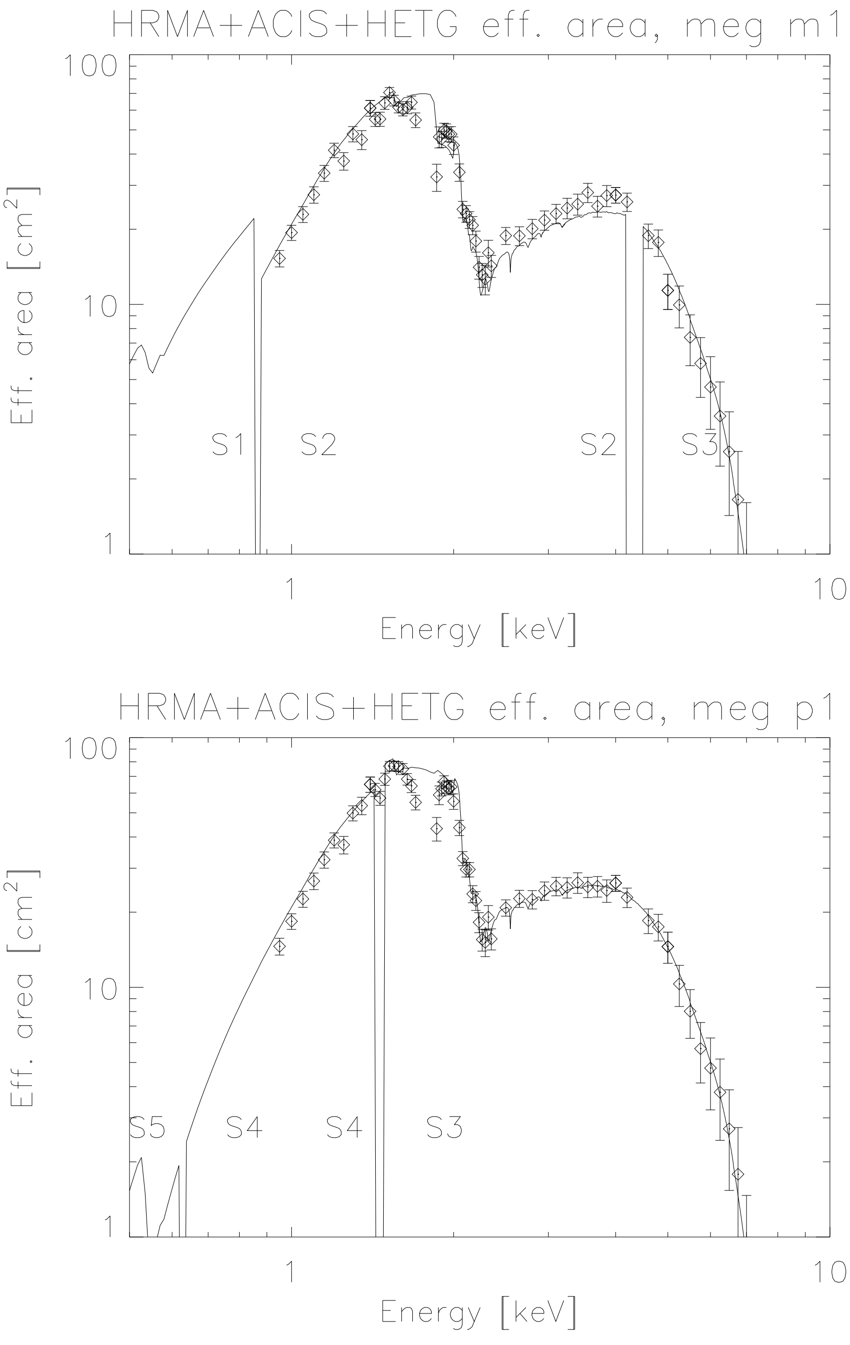

Figure 9. Comparison of measured absolute effective areas at XRCF of the MEG 1st order to the expected area distribution. Negative orders cover S2 and S3 (from low to high energies), the gap appears just above 4 keV. Positive orders cover S4 and S3 with the gap at 1.5 keV.

here without significance. Also in the -1st order above approximately 2.5 keV and below 4.2 keV, the measured areas stay consistently above the calculated function, again by only a small amount. All of these effects happen on CCDs, where we have used a template QE from a different device. The amount of these effect also matches the expected variation between the QEs for different devices. A strong argument against these effects being intrinsic to the grating itself is the fact that in +1st order the area between 2.5 keV and 4.2 keV matches precisely the expectation: this portion covers device S3, which is the template BI device.

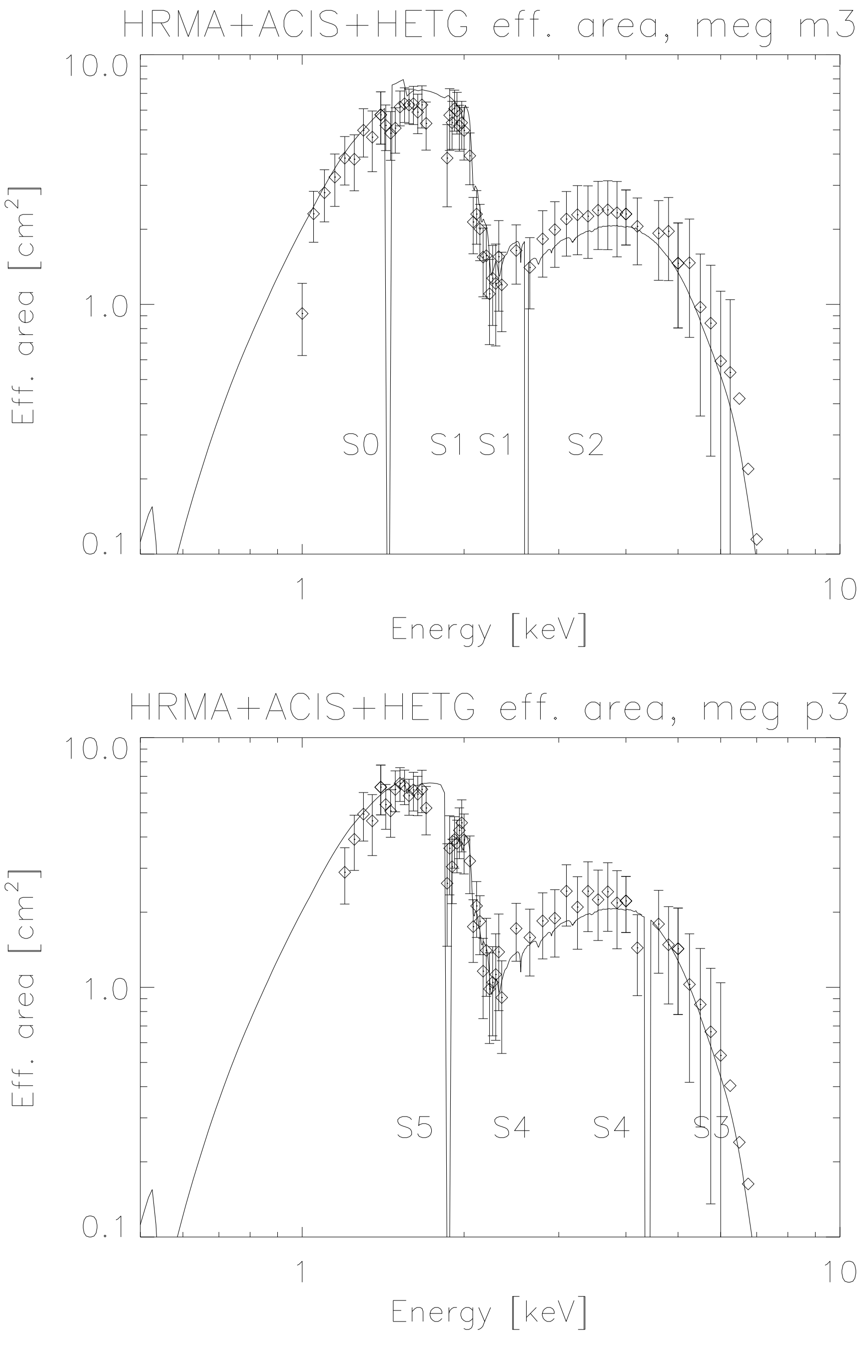

Figure 10. Measured absolute effective areas at XRCF of the MEG 3rd order.

Figure 10 shows the areas determined for the MEG 3rd orders. Again, except for a couple of data points, the general trend shows that the measured values match nicely the expectation. However, the statistics already limit the significance to less than 20%. Therefore we will not present higher order data in this context. Those results will be presented in terms of efficiency ratios for combined order by[8] in this volume.

5.3. 1st and 2nd order effective areas for the HEG

The bottom diagram of figure 5 shows the the subassembly expectation for the sum of the positive and negative 1st and 2nd HEG orders. The 2nd order efficiency, comparable to the 3rd order efficiency in the MEG, is low enough to

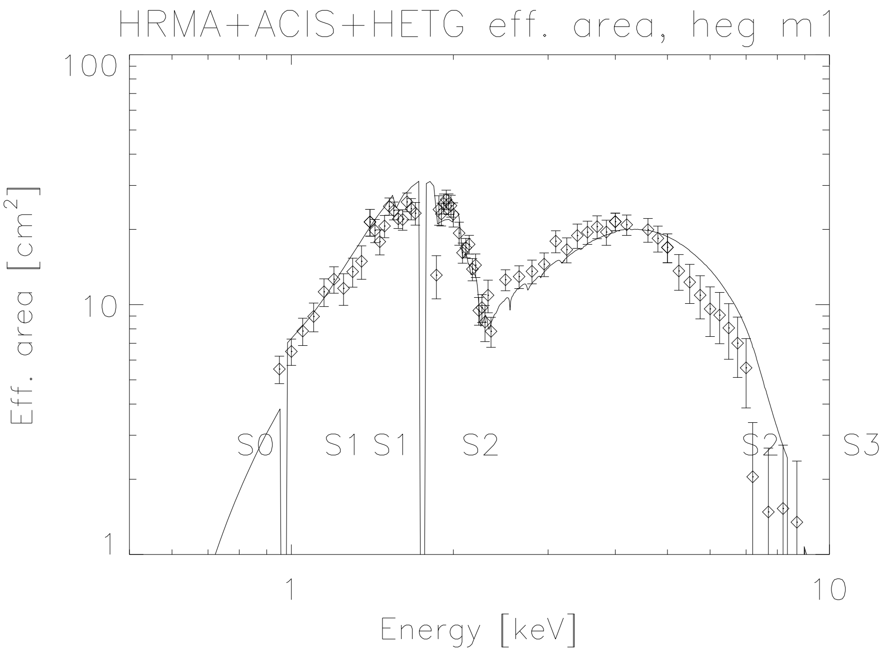

Figure 11. Comparison of measured absolute effective areas at XRCF of the HEG 1st order to the expected area distribution. Negative orders cover S1 and S2 (from low to high energies), the gap between the two appears 1.7 keV. Positive orders cover S5, S4, and S3 with the gaps at 1.3 and 2.9 keV respectively.

ensure that results will be not be affected by pile up. For the first order, we face a similar situation to the MEG first order, i.e. pile up is sufficiently corrected for by adding the 2-photon peak in the pulse heights back to the measured count rate. This peak is detectable thoughout the whole band pass.

Figure 11 shows the effective areas determined for the -1st (top, m1) and +1st (bottom, p1) order of the HEG. Note, that the HEG has considerably less efficiency below 2.5 keV than the MEG. Therefore counting statistics are

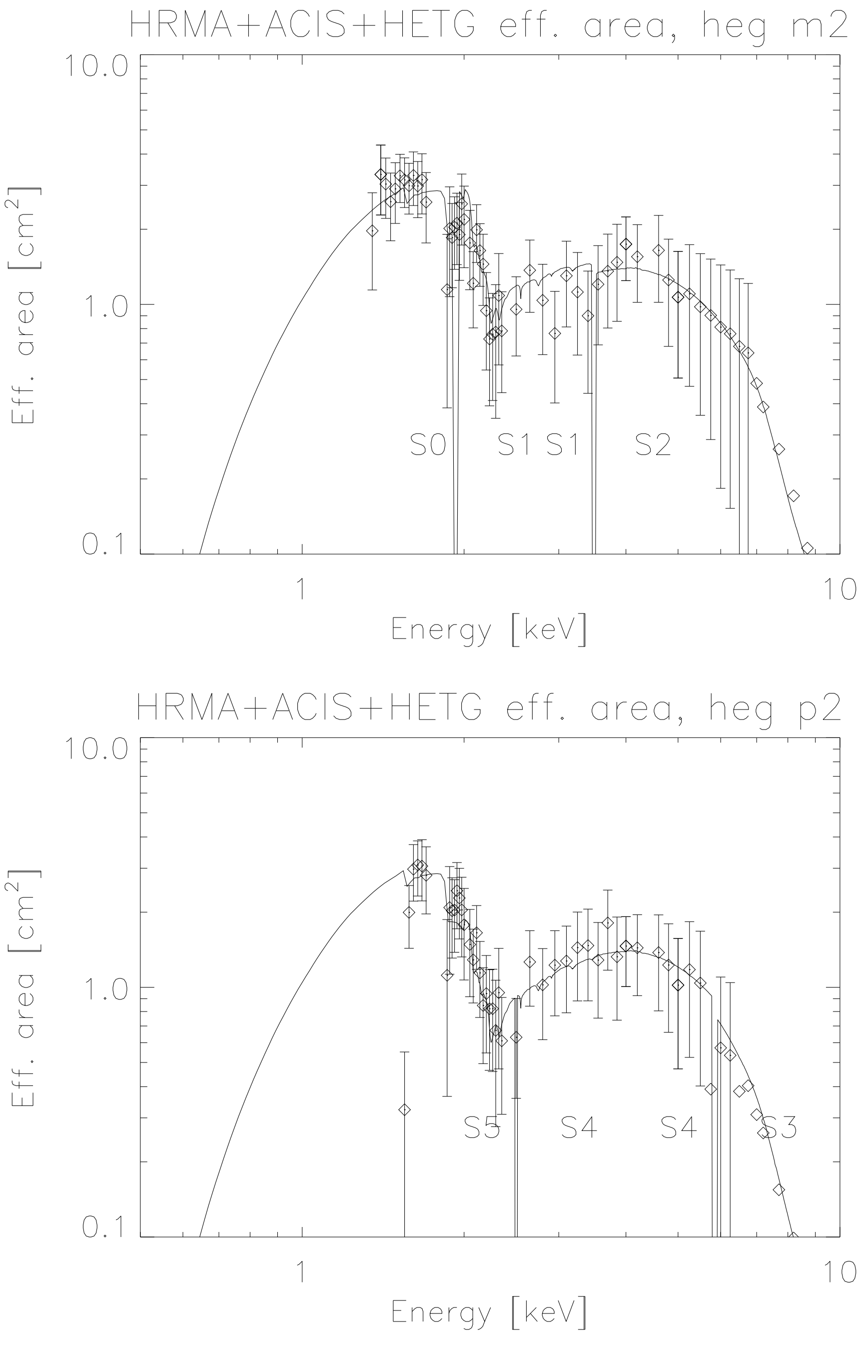

Figure 12. Measured absolute effective areas at XRCF of the HEG 2nd order.

worse than in the MEG. Below 1.5 keV we cannot determine the effective area better than 20%, above 1.5 keV and below 5 keV the uncertainties are of the order of 10-15%. Again the range around 1.75±0.15 keV is not reliable and should be disregarded.

Within the given uncertainties, the measured values again fit quite well with the expected function. At -1st order, like observed in the MEG the area between approximately 2.5 and 4.2 keV stay consistently above the expectation, which again points towards a slightly higher CCD efficiency at high energies in S2. A major effect is observed above 5 keV in both orders. Although the issue is not yet resolved, we suspect an anomalous local beam non-uniformity effect. Figure 7 shows that at this energy the FPC-T and FPC-N switch in relative intensity. The HEG entrance aperture is quite small in size and any local disturbance will effect the HEG image more than the MEG image. The MEG -1st order does show a similar trend at 5 keV, but at much lower scale.

Figure 10 shows the areas determined for the HEG 2nd orders. The measured values match the expectation. But like observed in the MEG 3rd orders, statistical uncertainties the significance to less than 20%. For higher order results we again refer to[8] in this volume.

6. CONCLUSIONS

We analysed effective area measurements performed at XRCF with the HETGS, by using the DCM energy scans in the energy range from 950 eV to 8700 eV. The measurements were designed to produce sufficient flux in the 1st and higher orders, therefore the 0th order measurements were dominated by pile-up effects. Table 2 summarizes the measured effective areas for a selected set of energies. The analysis resulted in the following:

E	0th	MEG 1	MEG -1	MEG 3	MEG -3	HEG 1	HEG -1	HEG 2	HEG -2
eV	cm^2	cm^2	cm^2	cm^2	cm^2	cm^2	cm^2	cm^2	cm^2
1000	58.9±2.5	18.3±1.1	19.4±1.4	0.0±0.0	0.9±0.3	4.9±0.7	6.5±0.8	–	–
	56.8	21.0	21.0	1.6	2.0	4.6	7.3	1.0	1.0
1200	53.6±3.3	38.8±2.7	41.5±2.8	2.9±0.7	3.9±0.8	11.9±1.5	12.6±1.5	–	–
	56.5	40.4	40.4	4.0	4.0	9.1	12.2	1.9	1.9
1400	56.7±4.6	65.0±4.6	61.1±4.4	6.3±1.4	5.7±1.4	21.3±2.6	21.4±2.6	–	3.3±1.0
	50.1	60.1	60.1	5.9	5.9	16.8	20.4	2.5	2.5
1610	48.4±3.1	75.0±3.8	60.3±3.4	6.2±1.0	6.4±1.1	24.2±2.2	21.9±2.1	3.0±0.8	3.3±0.8
	51.0	75.0	66.5	6.4	7.2	24.1	27.2	2.7	2.7
2140	95.0±3.8	29.6±2.0	21.8±1.7	1.8±0.5	2.0±0.5	16.7±1.5	17.4±1.5	1.1±0.4	1.6±0.5
	94.3	27.5	18.9	1.7	2.5	14.5	14.5	1.0	1.5
2500	74.0±3.0	20.8±1.6	18.8±1.5	1.7±0.4	1.6±0.4	12.2±1.2	12.6±1.2	0.6±0.3	1.0±0.3
	80.0	20.8	16.1	1.4	1.8	10.5	10.5	0.8	1.2
3100	94.9±4.1	25.4±2.2	23.1±2.1	2.4±0.7	2.2±0.6	17.8±1.8	17.9±1.8	1.3±0.5	1.3±0.5
	93.2	24.6	21.2	1.8	1.8	17.3	14.9	1.2	1.4
4000	129.6±4.2	26.2±1.9	27.4±2.0	2.2±0.6	2.3±0.6	19.7±1.7	21.5±1.7	1.5±0.5	1.7±0.5
	134.9	24.5	23.1	2.0	2.0	20.7	19.5	1.4	1.4
5000	131.5±6.11	14.6±2.1	11.4±1.8	1.4±0.6	1.5±0.7	14.7±2.1	16.9±2.2	1.0±0.5	1.1±0.6
	149.5	14.6	14.5	1.3	1.3	17.8	18.7	1.2	1.2
6000	122.7±7.6	4.7±1.5	4.7 ±1.5	0.5±0.5	0.6±0.5	7.7±1.9	9.6±2.2	0.6±0.5	0.8±0.6
	105.7	5.0	5.0	0.4	0.5	11.7	13.8	0.7	0.8
7000	53.7±5.3	0.8±0.7	0.9 ±0.7	0.1±0.2	0.1±0.2	4.8±1.6	5.6±1.7	0.3±0.4	0.5±0.5
	56.7	0.8	0.8	0.1	0.1	6.2	8.0	0.4	0.5
8200	16.0 ±3.8	0.1±0.3	0.0 ±0.2	0.0±0.1	0.0±0.1	1.5±1.2	1.5±1.2	0.1±0.3	0.2±0.4
	21.2	0.0	0.0	0.0	0.0	1.9	2.7	0.1	0.1

Table 2. Table of results of measured versus predicted effective areas if the HETGS for selected energies. The stated uncertainties include only counting statistics and BND uncertainties. The second row for each energy lists the expected effective area from the HRMA XRCF model and the ACIS and HETG subassembly predictions. Note, that because the predictions are derived from subassembly data, they itself have an uncertainty of up to 5%.

- The absolute effective area of the combined 0th order in MEG and HEG was measured to an accuracy better than 5% in the range 0.9 and 3.0 keV. The larger uncertainties were introduced by systematic errors from the DCM. At energies above 3 keV the measurements were entirely dominated by pile-up effects and the effective area in this range could only be verfied with an uncertainty above 20%
- The absolute effective areas of the 1st orders were determined with an accuracy between 5 and 10% for the MEG and between 10 and 15% for the HEG over most of the energy range. Above ∼5 keV counting statistics degrades significantly.

• The measured areas in the 1st orders for the MEG and HEG match the expectation from the XRCF HRMA measurements combined with the subassembly results for the ACIS-S and the HETG to quite a high degree. In detail: the MEG -1st order data from device S2 revealed significant variations that could be traced to variations in quantum efficency of device S2 in ACIS-S with respect to the applied QE template; the HEG measurements above 5 keV seem to be affected by local beam non-uniformities. A careful evaluation is still in progress.

• Although dominated by large statistical uncertainties the measured effective areas for the MEG 3rd and the HEG 2nd orders are very well in agreement with the expectation.

For the future this analysis has to be complemented by XRCF measurements using the single line sources, which allow us to study the energy range below 0.9 keV as well as the 0th order at high energies under less piled-up conditions. The DCM results for the HEG 1st order have to be fine tuned at high energies by including the measured beam unifomity maps. The 1st order results for both grating types should be refined by applying the actual QE functions for each CCD in the detector array as soon as they become available. Finally the grating results should be cross-calibrated with ACIS stand-alone measurements performed at XRCF. From the results of this analysis and once the outstanding issues are resolved, we will be able to refine our grating models in order to accurately predict the in-flight HETGS absolute effective area.

7. ACKNOWLEDGEMENTS

The authors want to thank Doug Swartz and the Project Science analysis team for a thorough analysis of the BND data. Thanks also to Kester Allen, Paul Plucinsky, and Brian McNamara for their help in dealing with the 0th order pile-up analysis, Dave Huenemoerder for carefully reading the manuscript. This work was supported in part by NASA under the HETG contract NAS-38249 and the AXAF Science Center contract to the Smithsonian Astrophysical Observatory, NAS8-39073.

REFERENCES

1. C.L. Allen, P.P. Plucinsky, B.R. McNamara, R.J. Edgar, N.S. Schulz, and and J.W. Woo, "Analysis of the AXAF HRMA+ACIS effective area measurments from the XRCF" *X-Ray Optics, Instruments, and Missions*, Proc. SPIE, Vol. **3444** (this volume), (1998).
2. M. Bautz, J. Nousek, G. Garmire and the ACIS instrument team, "Science Instrument Calibration Report for the AXAF CCD Imaging Spectrometer (ACIS)", available at at *http://wwwastro.msfc.nasa.gov/xray/axafps.html* (1997)
3. M.W. Bautz, F. Baganoff, T. Isobe, S.E. Jones, S.E. Kissel, B. LaMarr, H.L. Manning, M. Pivovaroff, G.Y. Prigozhin, J.A. Nousek, C.E. Grant, K. Nishikida, F. Scholze, R. Thornagel, and G. Ulm, "X-Ray CCD Calibration for the AXAF CCD Imaging Spectrometer", *X-Ray Optics, Instruments, and Missions*, Proc. SPIE, Vol. **3444**, (1998).
4. J.E. Davis, H.L. Marshall, M.L. Schattenburg, and D. Dewey, "Analysis and Modeling of Anomalous Scattering in the AXAF HETGS", *X-Ray Optics, Instruments, and Missions*, Proc. SPIE, Vol. **3444**, (1998).
5. D.Dewey, D.N. Humpheries, G.Y. McLean and D.A. Moschella, "Laboratory Calibration of X-ray Transmission Diffraction Gratings", *EUX, X-Ray, and Gamma-Ray Instrumentation for Astronomy V*, Proc. SPIE, Vol. **2280**, 257–271 (1994).
6. D. Dewey, H.L. Marshall, K.A. Flanagan, C. Baluta, C.R. Canizares, D.S. Davis, J.E. Davis, T.T. Fang, D.P. Huenemoerder, J.H. Kastner, N.S. Schulz, M.W. Wise, J.J. Drake, J.Z. Juda, M. Juda, A.C. Brinkman, T. Gunsing, J. Kaastra, G. Hartner and P. Predehl, "Towards the Callibration of the HETG Effective Area", *Grazing Incidence and Multilayer X-Ray Optical Systems*, Proc. SPIE, Vol. **3113**, 144–159 (1997)
7. K.A. Flanagan, D. Dewey, L. Bordzol, "Calibration and Characterization of HETG grating elements at the MIT X-ray Grating Evaluation Facility", *SPIE Proceedings* **2518**, 438–456 (1995).
8. K.A. Flanagan, N.S.Schulz, G.D. Hartner, and P. Predehl, "HETG High-Order Diffraction Efficiency" *X-Ray Optics, Instruments, and Missions*, Proc. SPIE, Vol. **3444** (this volume), (1998).
9. J.J. Kolodziejczak, R.A. Austin, R.F. Elsner, M.K. Joy, M. Sulkanen, E.M. Kellogg, and B.J. Wargelin, "X-Ray Source System at the MSFC X-Ray Calibration Facility", *X-Ray and Extreme Ultraviolet Optics*, Proc. SPIE, Vol. **2515**, 420–435 (1995).

10. T.H. Markert, C.R. Canizares, D. Dewey, M. McGuirk, C. Pak, and M.L. Schattenburg, "The High Energy Transmission Grating Spectrometer for AXAF", *EUX, X-Ray, and Gamma-Ray Instrumentation for Astronomy V*, Proc. SPIE, Vol. **2280**, 168–180 (1994).
11. H.L. Marshall, D. Dewey, K.A. Flanagan, C. Baluta, C.R. Canizares, D.S. Davis, J.E. Davis, T.T. Fang, D.P. Huenemoerder, J.H. Kastner, N.S. Schulz, M.W. Wise, J.J. Drake, J.Z. Juda, M. Juda, A.C. Brinkman, C.J.Th. Gunsing, and J.S. Kaastra, G. Hartner and P. Predehl, "Towards the Calibration of the HETG LRF", *Grazing Incidence and Multilayer X-Ray Optical Systems*, Proc. SPIE, Vol. **3113**, 160–171 (1997).
12. M. Weisskopf, R.F. Elsner, S.L. 0'Dell and the AXAF Project Science team, "Calibration of the Advanced X-ray Astrophysics Facility: Project Science analyses" available at at *http://wwwastro.msfc.nasa.gov/xray/axafps.html* (1997)
13. AXAF Science Center, "AXAF Observatory Guide",Rev. 1.0,available at *http://asc.harvard.edu* (1997)
14. M.D. Stage and D. Dewey, "Verifying the HETG Spectrometer Rowland Design", *X-Ray Optics, Instruments, and Missions*, Proc. SPIE, Vol. **3444**, (1998).
15. D.A. Swartz, R.F. Elsner, J.J. Kolodziejczak, S.L. O'Dell, A.F. Tennant, M.E. Sulkanen, M.C. Weisskopf, and R.J. Edgar, "Use of Monochromators for the Calibration of AXAF", *X-Ray Optics, Instruments, and Missions*, Proc. SPIE, Vol. **3444**, (1998).
16. M.C.Weisskopf and S.L. O'Dell, "Calibration of the AXAF observatory: overview", *Grazing Incidence and Multilayer X-Ray Optical Systems*, Proc. SPIE, Vol. **3113**, 2–17 (1997).
17. M.C.Weisskopf and S.L. O'Dell, "Calibration of AXAF: overview", *X-Ray Optics, Instruments, and Missions*, Proc. SPIE, Vol. **3444**, (1998).